Scaling-Based Design Approach for Tailbeat Fish-Inspired Robots Swimming at High Speed and Propulsive Efficiency

Khanh Nguyen[1], Hoon Cheol Park[2*]

[1,2]Laboratory of Bio-Inspired Systems, [1]Department of Smart Vehicle Engineering, [2]Department of Aerospace-Mobility Engineering, [1,2]Future Drone Center, Konkuk University, Seoul 05029, Republic of Korea.

[*]Corresponding author. Email : hcpark@konkuk.ac.kr

Integrating multiple parameters synchronously into the development of high-speed robotic fish remains a challenge. This explains why most existing fish-like robots have developed through trial-and-error methods. This paper presents a comprehensive scaling-based design approach for developing a 0.32-m-long robot, KUFish-II, capable of achieving a target speed of 1.75 m/s. This speed was first determined from a given body length and a Froude number of one, representing typical fast swimming, and then averaged with speeds computed using two additional metrics: the Strouhal number (St) and reduced frequency. The target frequency was set at 11.5 Hz, close to the reference tailbeat frequency of KUFish. For this purpose, a caudal fin with twice the area of that used in KUFish was designed to generate a thrust of 1.91 N at 11.7 Hz. In tethered experiments, KUFish-II generated a thrust of 1.99 N at the required frequency. Using a 30-V battery package, the robot reached a maximum free-swimming speed of 1.79 m/s at 12.20 Hz, producing 2.07 N and consuming 31.7 W. With the relatively small cost of transport (17.7 J/m) and low St (0.28), KUFish-II ranks among the most efficient robotic swimmers reported to date. These results confirm the reliability of the proposed approach in thrust, frequency, and swimming speed predictions, and highlight its potential for larger, fast-swimming tailbeat robots.

1. Introduction

Fish locomotion has been extensively explored over the past several decades (Salazar et al., 2019; Sfakiotakis et al., 1999; Webb, 1988). However, despite technological advancements, fully understanding the swimming mechanics of fast-swimming oceanic species (Ren and Yu, 2021; Walters and Fierstine, 1964) remains challenging. Thus, fast-swimming fish have always been a major source of inspiration for researchers aiming to reproduce their fast-swimming behavior in robotic fish (Anderson and Chhabra, 2002; Clapham and Hu, 2015, 2014; Hu et al., 2015; Iguchi et al., 2024; Pham et al., 2023; Tsimbo Fokou et al., 2023; Wang et al., 2010; Wen et al., 2013; White et al., 2021; Yu et al., 2016; Zhong et al., 2021, 2017; Zhu et al., 2019). In addition, gaining deeper insights into the swimming behavior of natural underwater species is essential for improving the interaction between artificial aquatic bodies and their surrounding water environments. For real ocean applications, a robotic fish must be able to swim forward to overcome a stream under the sea whose speed can reach 2.5 m/s near the sea surface (Driscoll et al., 2008). Thus, the maximum swimming speed of a robotic fish should be higher than the stream speed under the sea, because a robotic fish can encounter such a fast stream. Therefore, a fast-swimming fish can provide useful insights to design a robotic fish for practical applications (Raj and Thakur, 2016). To achieve high speed and fast acceleration, fish typically undulate their bodies and beat the caudal fin (CF), which is known as the BCF mode, rather than using the median and/or paired fins (MPF mode), which generate relatively smaller thrust, and thus result in slower swimming (Breder, 1926; Sfakiotakis et al., 1999).

In the oceanic environment, aquatic species can reach swimming speed exceeding 20.0 body lengths per second (BL/s) while exhibiting a wide range of tailbeat frequencies from 0.1 to 20.0 Hz (Bainbridge, 1958). Notably, the yellowfin tuna, a thunniform fish (Shadwick and Syme, 2008), can reach a maximum speed of 20.8 m/s (21.1 BL/s) (Walters and Fierstine, 1964), which is significantly higher than that achieved by any fish-inspired robotic platform to date. Indeed, current robotic fish prototypes have yet to match the swimming speeds of real fish. For example, the iSplash-I can swim at 0.7 m/s (2.8 BL/s) (Clapham and Hu, 2014), Tunabot at 1.02 m/s (4.0 BL/s) (Zhu et al., 2019), the single-motor-actuated fish at 1.14 m/s (3.1 BL/s) (Yu et al., 2016), Tunabot Flex at 1.17 m/s (4.6 BL/s) (White et al., 2021), the VCUUV at 1.25 m/s (0.5 BL/s) (Anderson and Chhabra, 2002), KUFish at 1.40 m/s (6.4 1 BL/s) (Pham et al., 2023), SPC-3 UUV at 1.87 m/s (1.2 BL/s) (Wang et al., 2010), the robotic thunniform swimmer at approximately 2.0 m/s (1.7 BL/s) (Hu et al., 2015), and the agile robotic fish at 2.6 m/s (6.3 BL/s) (Iguchi et al.,

2024). Despite efforts to reproduce thunniform swimming, a form of low-drag undulatory motion with increasing flexibility toward the posterior, Tunabot can achieve a maximum tailbeat frequency of 15.0 Hz but only reaches a swimming speed of approximately 1.0 m/s (Zhu et al., 2019). To the best of our knowledge, the iSplash-II (Clapham and Hu, 2015), which mimics carangiform locomotion, characterized by undulations with slightly larger body angles than the thunniform mode, is recognized as the fastest humanmade tailbeat robot, achieving a maximum speed of 3.7 m/s (11.6 BL/s) at the fastest tailbeat frequency of 20.0 Hz and even outperforming actual carangiform fish (Clapham and Hu, 2015). However, creating fast swimming on a robotic platform is a challenging task that requires a detailed study of aquatic locomotion, body shape design, and tailbeat patterns (Dean and Bhushan, 2010; Rossi et al., 2011; Zhong et al., 2021), which include variations in tailbeat frequency, stroke amplitude, tail deformation, and stiffness.

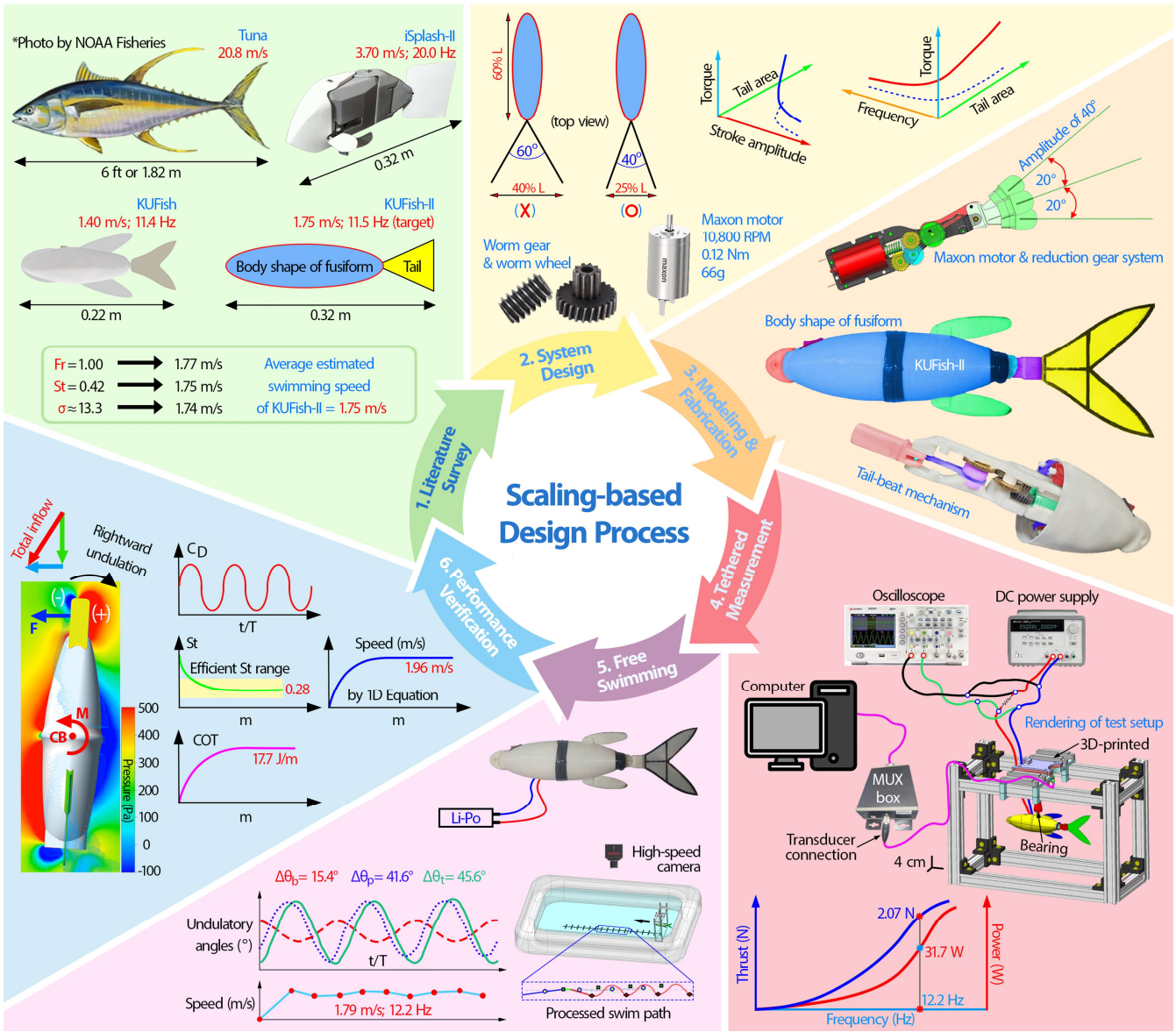

Fig. 1. Diagram of the six-step scaling-based design process for tailbeat robotic fish. The process begins with a literature survey to determine the target swimming speed. The system design phase searches for the suitable CF area and computes the required thrust and torque, tailbeat frequency, and tailbeat stroke amplitude. The fabrication step illustrates the CAD modeling and final KUFish-II model. Tethered and free-swimming experiments are conducted to validate the design, followed by the performance verification and analysis.

While making efforts to achieve high swimming speeds, improving swimming efficiency by reducing body drag is another common concern (Bartol et al., 2003; Dean and Bhushan, 2010; Jaya and Kartidjo, 2022; Lindsey, 1978; Matta et al., 2020; Yu et al., 2020). Extensive studies have been conducted on practical applications to minimize body drag, including replication of the most efficient thunniform mode (Hu et al., 2015; Matta et al., 2020; Shadwick

and Syme, 2008; Zhu et al., 2019), the most common fish carangiform mode (Clapham and Hu, 2015; Lucas et al., 2020; Wen et al., 2013), and body shape optimization (Bartol et al., 2003; Dean and Bhushan, 2010). Among these approaches, the adoption of a fusiform body (wide at the midsection and streamlined at both ends) is widely regarded as the most effective for high-speed achievement, as it minimizes flow separation along the body (Lindsey, 1978).

More importantly, thrust increase is critical for faster swimming, and numerous studies have examined the CF mechanisms for thrust enhancement. For example, (Drucker and Lauder, 2001) experimentally concluded that the oscillatory motion of dorsal fin, whose phase was 30% advanced relative to the CF, contributed to a 12% thrust increase owing to a reverse von Kármán vortex street. Similarly, computational fluid dynamics (CFD) simulation in (Liu et al., 2017) indicated that the flow structures generated by median fins enhanced the leading-edge vortex (LEV) around the CF, explaining a 10%–20% increase in thrust. Also, by incorporating median fins into the body fairing (BF), the total drag was reduced by 20% compared with the models without median fins.

Considering these factors, the tuna, with its fusiform body shape and thunniform locomotion, represents a promising candidate model for designing fast-swimming robots (Barrett, 1996). However, replicating its swimming speed is challenging due to motor torque and speed limitations. The motor mass is another design parameter because a robotic fish should achieve neutral buoyancy for agile swimming. A robot with a heavier motor requires a larger body for neutral buoyancy, producing a higher drag. Thus, selecting a lightweight motor with adequate torque and speed is key for achieving the required frequency and thrust, and for further reducing body drag (Youssef et al., 2022).

Unfortunately, we could not find articles describing a complete systematic design procedure for robotic fish that incorporates the key considerations and predictions of the target swimming speed, required tailbeat frequency and torque, motor selection, neutral buoyancy, and other related factors. Therefore, it appears that the existing fast-swimming robotic fish (Clapham and Hu, 2015; Iguchi et al., 2024; Pham et al., 2023; Tsimbo Fokou et al., 2023; Wang et al., 2010; Wen et al., 2013, 2010; White et al., 2021; Zhong et al., 2017; Zhu et al., 2019) have been developed through a trial-and-error approach. In this study, we proposed a scaling-based design approach to develop a robotic fish with a given body length. Using three physical parameters of the Froude number (Fr), Strouhal number (St), and reduced frequency (σ), we first estimated the maximum swimming speed as the average of the speed calculated with a Fr of one and the two additional speeds estimated from the St and σ, along with a feasible tailbeat frequency. To achieve this speed, scaling relationships were then applied to predict the key design parameters, such as the required thrust, torque, tailbeat stroke amplitude and CF area, enabling the robotic fish to swim at the target maximum speed and tailbeat frequency. Thus, our proposed scaling-based design differs from the existing scaling laws (Floryan et al., 2018, 2017; Yu and Huang, 2021). For example, Ref. (Yu and Huang, 2021) introduced a scaling relationship describing fish undulatory propulsion, in which thrust was related to undulating wavelength, wave amplitude, and swimming speed, while the CF area and tailbeat stroke amplitude were not explicitly considered. Meanwhile, in the analysis of foil performance in (Floryan et al., 2018, 2017), the scaling of thrust was related to the area of oscillating airfoils and the square of speed, while the tailbeat stroke amplitude was identified as a source of viscous drag, adding a negative offset to thrust at a low oscillating frequency.

For validation of our proposed scaling-based approach, we developed a 0.32-m-long robotic fish, namely, KUFish-II, capable of achieving a target swimming speed of 1.75 m/s, applying the proposed approach. More details of defining the target swimming speed are presented in Section 2.1. A complete six-step design process, from literature survey to swimming verification, is illustrated in Fig. 1. The development of KUFish-II first followed the proposed design approach based on the reference parameters from our previously developed KUFish (Pham et al., 2023) and the target swimming speed, which was computed using literature-informed values of the Fr, St, and σ (Anderson et al., 1998; Bandyopadhyay, 2002; Belmonte et al., 1998; Eloy, 2012; Taylor et al., 2003). Additional parameters, including mass, volume, body wetted area, tail fin area, tailbeat amplitude, and required torque and thrust production, were predicted using this scaling-based relationship. In addition, the proposed design was validated through both tethered and free-swimming tests, including the measurements of frequency, thrust, power consumption, undulatory swimming kinematics, and free-swimming speed. Finally, the body drag coefficient was computed by CFD, and the swimming speed and distance were examined by a one-dimensional (1D) equation of motion.

2. Materials and Methods

2.1. Scaling-based design approach for tailbeat mechanism

This study focused on providing a complete approach for designing a tailbeat robotic fish that can reach a specified swimming speed. As a starting point, we address the question: How fast can the 0.32-m-long KUFish-II swim while achieving high efficiency? We review the literature-informed values for three metrics commonly used to characterize the swimming performance of aquatic species: the Froude number, Strouhal number, and reduced frequency. The first consideration is the Froude number, defined as $Fr = U/(gL)^{-0.5}$, where U is the maximum swimming speed (m/s), g is the Earth's gravity (m/s^2), and L is the body length (m). This metric is used to evaluate the characteristics of fluttering motions, describe the relationship between inertial and gravitational forces, and characterize the maneuverability of swimming. Previous studies (Bandyopadhyay, 2002; Belmonte et al., 1998) have shown that objects featuring long lightweight strips with oscillatory motion can achieve a Fr of up to 1.0. However, most robotic fish swim at Fr < 1.0. For example, the ACPM robot swims at a Fr of 0.38 (Zhong et al., 2017), iSplash-I at 0.45 (Clapham and Hu, 2014), SPC-3 UUV at 0.47 (Wang et al., 2010), Tunabot at 0.64 (Zhu et al., 2019), Tunabot Flex at 0.74 (White et al., 2021), and KUFish at 0.95 (Pham et al., 2023). Outperforming these robots, the agile robotic fish swam at a Fr of 1.29 (Iguchi et al., 2024) and iSplash-II at 2.09 (Clapham and Hu, 2015), indicating that their motion was always in the burst-swimming regime (Bandyopadhyay, 2005).

Another prominent factor in analyzing swimming modes is the Strouhal number (St) (Sfakiotakis et al., 1999), which is defined as $St = fA_m/U$, where f is the tailbeat frequency (Hz) and A_m is the CF's peak-to-peak amplitude (typically $A_m < 0.25L$ (Bainbridge, 1958)). The St reflects the wake dynamics of swimming animals (Triantafyllou et al., 1991) and represents the speed at which the tail beats relative to forward swimming speed (Lauder and Tytell, 2005). Later studies have shown that both swimming and flying animals (Eloy, 2012; Taylor et al., 2003) generally achieve energy-efficient motion within the same range of 0.25 < St < 0.35. For robotic fish, except for the agile robotic fish (St ≈ 0.3) (Iguchi et al., 2024), iSplash-II (St ≈ 0.34) (Clapham and Hu, 2015), and ACPM fish robot (St ≈ 0.36) (Zhong et al., 2017), most robotic fish swim at higher St than natural swimmers, such as around 0.4 for Tunabot (Zhu et al., 2019) and iSplash-I (Clapham and Hu, 2014), 0.43 for Wen's carangiform (Wen et al., 2013), 0.45 for both KUFish (Pham et al., 2023) and SPC-3 UUV (Wang et al., 2010), 0.46 for Tunabot Flex (White et al., 2021), and 0.63 for SoRoFAAM-1 (Tsimbo Fokou et al., 2023).

The third metric is the reduced frequency σ, which represents the acceleration reaction to hydrodynamic forces and relates the period of a water particle traversing along the body length to the period required for a complete tailbeat cycle (Webb, 1988). It is defined as $\sigma = 2f\pi L/U$. Typically, the reduced frequency for aquatic animals falls within the range of 0.1 to 0.4, which indicates both acceleration reaction and hydrodynamic force components contributing to the force balance (Webb, 1988). However, for robotic swimmers, the reduced frequency far exceeds the value of 0.4. For example, σ is approximately 10.8 for iSplash-II (Clapham and Hu, 2015), 10.9 for Tunabot flex (White et al., 2021), 11.2 for KUFish (Pham et al., 2023), 13.4 for SPC-3 UUV (Wang et al., 2010), 14.9 for iSplash-I (Clapham and Hu, 2014), and 23.6 for Tunabot (Zhu et al., 2019), indicating that these robots pursue acceleration reaction for fast locomotion.

As our objective is to create a fast-swimming robot capable of reaching a Fr of 1.0, the swimming speed computed using this value, which depends solely on body length, serves as a reference for calculating two other speeds using the St and σ parameters. This is because computing speeds using St and σ requires two other design parameters: f and A_m for St, and f and L for σ. Thus, with a target body length of 0.32 m, the maximum swimming speed of the KUFish-II was estimated to be 1.77 m/s using a Fr of 1.0. Given the reported values of St and σ, we assumed a tailbeat frequency (f = 11.5 Hz) and peak-to-peak amplitude $(A_m = 0.2L)$ to achieve similar maximum speeds of 1.77 m/s. The resulting estimated speeds were 1.75 m/s (using St = 0.42) and 1.74 m/s (using σ = 13.3). These three estimated swimming speeds suggested an average target swimming speed of 1.75 m/s (5.5 BL/s). See the predicted values in Table A1 for details. Nevertheless, this raises a question about the effect of choosing a tailbeat frequency different from 11.5 Hz, such as 5.0 or 20.0 Hz. For a selection of 5.0 Hz, while maintaining the same L

and A_m, the parameters of Fr = 1.0, St = 0.18, and σ = 5.8, are selected, which result in the possible swimming speeds of 1.77, 1.75, and 1.73 m/s, respectively. In this case, the average swimming speed is again 1.75 m/s. Although these computed swimming speeds are close to each other with small differences, both the selections of σ = 5.8 and St = 0.18 fall beyond the typical ranges reported for swimming robots. This indicates a feasible limitation of such low-frequency designs. Similarly, at a higher frequency of 20.0 Hz and with the same L and A_m, the set of (Fr = 1.0, St = 0.74, and σ = 23.0) is selected to achieve the same target speed of 1.75 m/s. However, St = 0.74 far exceeds its optimal range, and σ = 23.0 is significantly high, indicating an unfeasibly high-frequency design under the current assumptions. Therefore, to predict the possible swimming speed, it is important to choose design parameters, such as the body length tailbeat frequency, and peak-to-peak amplitude, such that three parameters Fr, St, and σ fall within feasible ranges at the preliminary design stage.

Here, we describe a scaling-based design approach to determine design parameters, such as the body surface area, volume, and mass of the KUFish-II. All the reference parameters of the KUFish (Pham et al., 2023) and the predicted data of the KUFish-II are summarized in Table A2. The reference parameters of the KUFish were scaled to predict those of the current KUFish-II design to ensure that a target speed of 1.75 m/s is achieved. More specifically, the robots were assumed to reach their maximum swimming speed and maintain constant speeds after $m\dot{U} = 0$, indicating that the thrust (T) and body drag (D) were balanced, as expressed by the following 1D equation:

$$T - D = m\dot{U}. \tag{1}$$

In Eq. (1), the body drag is defined as $D = 0.5\rho U^2 S C_D$, where ρ is the water djensity, S is the body surface area, and C_D is the drag coefficient during undulatory swimming. We assumed that the C_D of the KUFish-II remains identical to that of the KUFish $(C_D = 0.032)$ (Nguyen et al., 2022), whereas owing to the increase in motor mass, its assumed body mass (M_2) is 20% greater than that of the KUFish (M_1), corresponding to $M_2 = 1.2 \times M_1$. Consequently, for neutral buoyancy, the volume (V_2) of the KUFish-II should be increased by a factor of 1.2, and therefore, its body surface area (S_2) increases by $(1.2)^{2/3}$, compared with the corresponding V_1 and S_1 of the KUFish (Table A2). Using Eq. (1) when $\dot{U} = 0$ and the definition of drag, assuming the same C_D for the KUFish and KUFish-II, whose CF shapes are similar (Steps 1 and 3, Fig. 1) and aspect ratios are identical to 2.56 (computed by $AR = b^2/A$ (Sfakiotakis et al., 1999) in Table A2), the required thrust, T_2, of the KUFish-II is 1.91 N, which was calculated using Eq. (2) to achieve the predicted swimming speed, U_2.

$$T_2 = T_1 \times \frac{S_2}{S_1} \times \left(\frac{U_2}{U_1}\right)^2, \tag{2}$$

where the symbols with the subscripts "1" and "2" indicate the known parameters of the KUFish and the predicted parameters of the KUFish-II, respectively. Note that U_2 is the estimated target swimming speed (1.75 m/s) based on three physical parameters. To account for the relationship between the ratios of thrust (T_2/T_1) and the ratios of the CF area (A_2/A_1), tailbeat frequency (f_2/f_1), and tailbeat amplitude (θ_2/θ_1), Eq. (3) was derived from CFD results (Nguyen et al., 2023) as follows:

$$\frac{T_2}{T_1} = \left(\frac{A_2}{A_1}\right)^2 \times \left(\frac{f_2}{f_1}\right)^2 \times \left(\frac{\theta_2}{\theta_1}\right)^{2.15}, \tag{3}$$

where θ_2 is the desired tailbeat amplitude of the KUFish-II. Subsequently, for a selected A_2/A_1 and the computed ratios of thrust, frequency, and tailbeat amplitude, the predicted frequency f_2 was calculated using Eq. (4), as follows:

$$f_2 = f_1 \times \frac{A_1}{A_2} \times \sqrt{\frac{T_2}{T_1} \times \left(\frac{\theta_1}{\theta_2}\right)^{2.15}}. \quad (4)$$

Notably, A_2/A_1 should be selected such that the predicted f_2 from Eq. (4) closely matches the assumed or target frequency of 11.5 Hz, which is used to estimate the speeds based on the St and σ parameters (Step 1, Fig. 1). Then, this predicted f_2 is an input to estimate the required torque Q_2 in Eq. (5). For the calculation, we update the existing relationship of (Q_2/Q_1) as a function of (A_2/A_1) and (f_2/f_1), developed in (Nguyen et al., 2023), to account for the effect of change in stroke amplitude on torque using the added mass method in (Pham et al., 2023), as follows:

$$\frac{Q_2}{Q_1} = \left(\frac{A_2}{A_1}\right)^{2.5} \times \left(\frac{f_2}{f_1}\right)^{2} \times \left(\frac{\theta_2}{\theta_1}\right). \quad (5)$$

Using Eq. (5), the required torque Q_2 can be estimated by the selected A_2/A_1, predicted f_2, and desired θ_2. The data used to extract Eq. (3) and (5) are summarized in Tables B1 and B2, respectively, with detailed explanations provided in Appendix B. For motor selection, the predicted f_2 in Eq. (4) and the required torque Q_2 in Eq. (5) are compared with the available frequency $(f_{2,spec})$ and torque $(Q_{2,spec})$, respectively, computed from the motor specifications: the nominal speed (revolutions per minute, RPM) in Eq. (6) and the stall torque (Q_s) in Eq. (7).

$$f_{2,spec} = \frac{RPM}{60 \times GR}, \quad (6)$$

$$Q_{2,spec} = Q_s \times GR, \quad (7)$$

where GR is the reduction gear ratio. The process of design parameter analysis is detailed in Section 3.1.

2.2. Design and fabrication

The body of the KUFish-II contains eight key components: anterior and posterior body parts, an additional nose fin (NF) section for neutral buoyancy, a tailbeat mechanism, a support structure for the mechanism, a motor, two rear fins (RFs), and a CF (see Fig. 2A-D). The external body shape was inspired by a fusiform design (Lindsey, 1978). Except for the motor, reduction gear system, and CF, most components, including the BF, supporting frames, NF, and RFs, were fabricated from polylactic acid (PLA) using a 3D printer (Cubicon, South Korea). Thus, its body is rigid and stiffer than the body of tuna, which has numerous spinal joints that allow for greater bending. The CF was fabricated by cutting a 0.6-mm-thick glass/epoxy plate.

A four-bar linkage was used to transform the motor rotational motion into the reciprocating motion of the peduncle, where the CF was attached through the rigid joint (Fig. 2D). In Fig. 2A, the lengths of the coupler O_1O_2 and crank O_2O_3 required to create a tailbeat angle θ were calculated using the predetermined lengths of the linkages OO_1 and OO_3 by the equations reported in (Pham et al., 2023). In Fig. 2A-C, the DCX motor was secured between the upper and lower 3D-printed frames, and seven Li-Po batteries were connected in series to form a 26-V battery package. A worm gear and multiple reduction gears were used to organize the transmission with a specific gear ratio. The actual operation of the tailbeat mechanism is shown in Movie S1. The center of mass of the robot was experimentally aligned with the CB and positioned below the body centerline for passive roll stability (Aureli et al.,

2010; Pham et al., 2023). To prevent unwanted yaw and enhance the formation of LEV on the CF, the RFs were attached (Fig. 2C and D). With these arrangements, the KUFish-II can stably perform fast swimming, even without feedback control, and reach its maximum speed within a short time and distance. Waterproofing was achieved through the use of spray coating, waterproof tape, latex sheets, and epoxy.

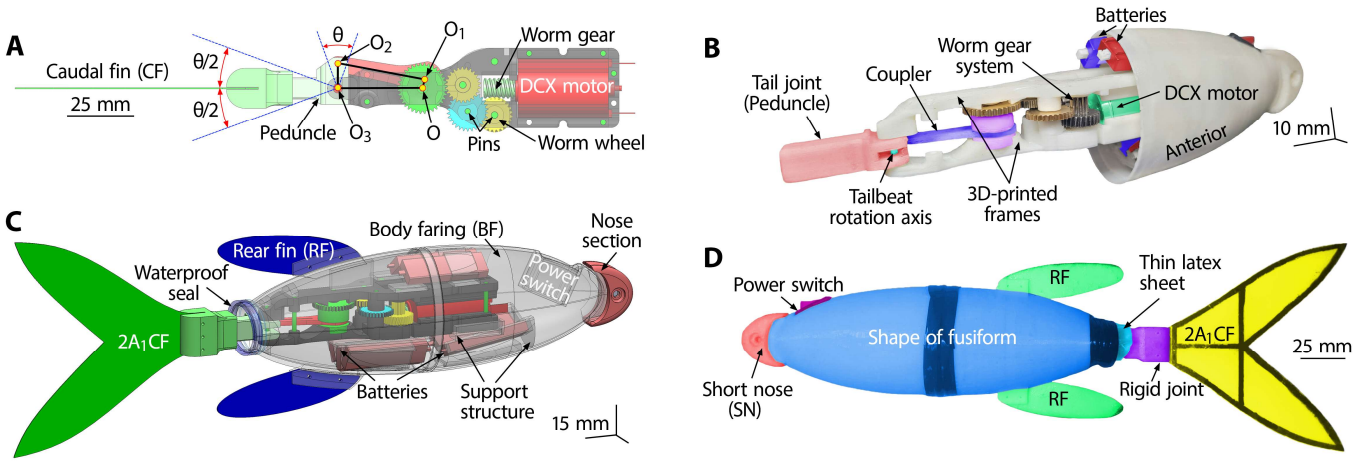

Fig. 2 Design and fabrication of KUFish-II. (**A-B**) Tailbeat mechanism: (A) rendering and (B) fabricated version with anterior fairing. (**C-D**) Fairing and CF: (C) rendering and (D) fabricated version.

2.3. Measurements of thrust and power consumption

The experimental setups for the frequency, thrust, power, kinematics, and swimming speed measurements are shown in Fig. 3A-C. In the tethered experiments (Step 4 in Fig. 1 and Fig. 3A), tailbeat motions were excited by an external DC power supply (Keysight E36103A, USA). The thrust generated by the CF was transmitted to a force transducer (ATI six-axis force/torque transducer, Gamma, SI 130-10, IP68, USA, force resolution of 0.025 N) via a 3D-printed coupling structure (Fig. 3A). The body could rotate symmetrically around the coupling structure using a stainless-steel ball bearing (C-SE608ZZ, Misumi, Japan). The force transducer was installed above the water surface and housed in a 3D-printed fixture mounted on a frame made of 40 cm × 40 cm aluminum profiles (Fig. 3A). The tailbeat frequency was measured by analyzing the recorded force signals.

The power consumption of the tailbeat mechanism was measured by calculating the product of the current passing through the motor and applied voltage. The current applied to the motor was measured using a resistor (R) and oscilloscope (TDS 2024, Tektronix Inc., USA; Step 4 in Fig. 1). Recorded within a 6-s display window, the voltage was sampled at 100 Hz for 1.5 to 2.5 s, corresponding to 15 to 25 tailbeat cycles. Then, the instantaneous power consumption at time t, $P(t)$, is computed using the instantaneous of the output voltage of the power supply, $Vol_1(t)$, and input voltage to the robot, $Vol_2(t)$, as follows:

$$P(t) = Vol_2(t) \times I(t) = Vol_2(t) \times \frac{Vol_1(t) - Vol_2(t)}{R}, \quad (8)$$

where $I(t)$ is the instantaneous current, and $Vol_1(t) - Vol_2(t)$ is the voltage across the resistor at time t.

Fig. 3B shows the setup for measuring the swimming speed and undulatory kinematics. The experiments were conducted in a pool measuring 2.5 m × 1.8 m × 0.4 m in length × width × height. A high-speed camera (HSC) (FASTCAM Mini UX50, Photron, Japan), which captured consecutive images with a pixel resolution of 1,280×1,024 at 250 Hz, was mounted two meters above the floor. To minimize the optical issues of capturing images across air-water media, the swimming speeds were measured within the focal area ranging from 0.6 to 1.2 m after the robot departs (Fig. 3B). A release mechanism, which was mounted on a 20 cm × 20 cm aluminum frame positioned along the pool centerline, held the robot and ensured a consistent posture at the start of swimming (Fig. 3B). The frame was adjusted to submerge the robot at the mid-plane of the water, approximately 0.2 m below the water surface. A

dummy mass was added to the nose section (Fig. 2C and D) to ensure neutral buoyancy and static balance. The recorded undulatory swimming was analyzed in MATLAB (MathWorks Inc., Natick, MA, USA) using the DLTdv-8 tool (Hedrick, 2008).

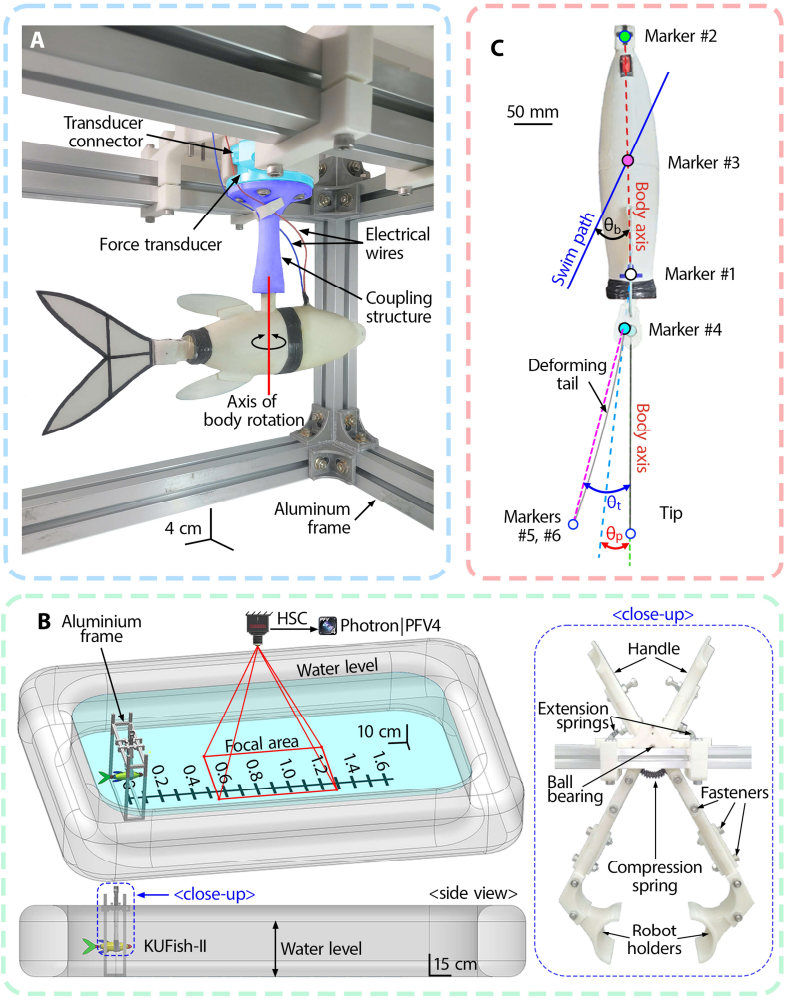

Fig. 3. Measurements of force, power, swimming speed, and undulatory kinematics. (**A**) Actual setup for the tethered experiments measuring force and power consumption (Step 4 in Fig. 1 for the CAD image). (**B**) Rendering of the experimental setup for measuring the free-swimming speed, with a close-up of the 3D-printed release mechanism. (**C**) Robot with tracking markers used for analyzing the undulatory kinematics.ss

To validate the design of the tailbeat mechanism, the midline kinematics of the KUFish-II were analyzed. In Fig. 3C, the 2D pixel-based trajectories of six markers along the symmetric body axis were tracked: #1 at the tailbeat rotation axis, #2 at the nose, #3 at the body midpoint, #4 at the point connecting the peduncle and CF, #5 at the upper tip, and #6 at the lower tip. Distinguishing the upper and lower tip points of the CF is necessary because of the body pitching motion. The swim path of the KUFish-II is defined by the initial and final tracked positions of marker #3 because of its minimal lateral fluttering during swimming. Therefore, the angle between the swim path and the body axis is defined as the body's undulatory angle θ_b. Because of the CF deformation, the full-stroke angle of the peduncle, θ_p, which is defined as the angle between the body axis (connecting markers #1 and #2) and the peduncle axis (connecting markers #1 and #4), is regarded as the designed stroke amplitude of the tailbeat mechanism, θ (Fig. 2A). Meanwhile, the angle formed by the line connecting marker #4 and markers #5 or #6 at the tip of the CF and the peduncle axis (an extended line connecting markers #1 and #4, Fig. 3C) is defined as the tail bending angle, θ_t. In this case, θ_t may vary depending on which marker (#5 or #6) is used to measure the angle because the motion of the two markers is not identical. Thus, tracking markers #5 and #6 were necessary. The defined bending angle θ_t is the average of the two angles computed using these two markers.

3. Results

3.1. Design parameters

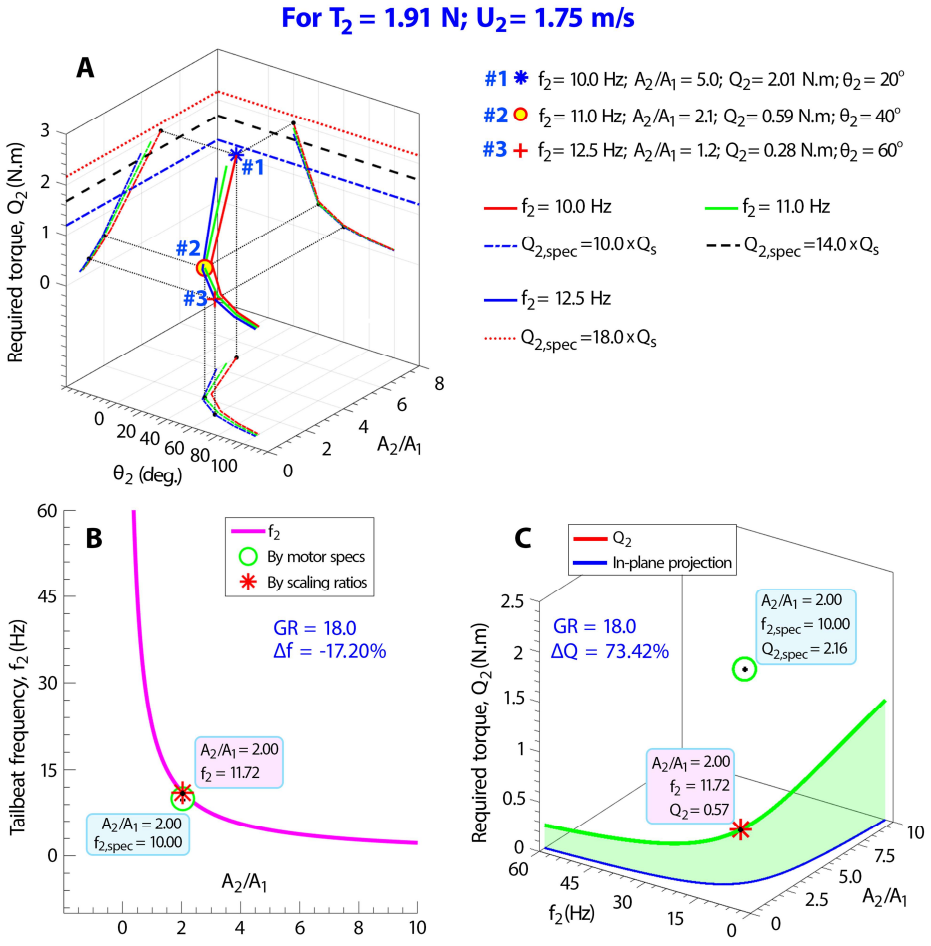

Fig. 4. System design. (**A**) Torque prediction from various tailbeat angles and CF areas at (10.0, 11.0, and 12.5) Hz. Three parallel dashed lines on two vertical planes are the available torques computed using Eq. (7). (**B-C**) Comparison of the (B) predicted and available frequencies using Eqs. (4) and (6), respectively, and the (C) required and available torques computed using Eqs. (5) and (7), respectively.

A design parameter study for the KUFish-II using Eqs. (1)–(5) is illustrated in Fig. 4A. Specifically, to produce the same required thrust, the required torque (Q_2) was examined for different CF area ratios (A_2/A_1), tailbeat amplitudes (θ_2), and frequencies (f_2). The CF must balance its size, tailbeat frequency, and stroke amplitude to generate sufficient thrust with least torque requirement. A higher-torque motor is required to drive the tailbeat mechanism, where a larger CF beats at a lower frequency and smaller amplitude (Fig. 4A). By contrast, a smaller fin with a larger stroke amplitude beating at a higher frequency should be considered for a smaller torque requirement. For example, to produce a thrust of 1.91 N, a CF beating at 10.0 Hz with a stroke amplitude of 20° requires a CF area five times larger than A_1, along with a driving torque of 2.01 N.m (#1, Fig. 4A). Note that A_1 is the caudal fin area of KUFish, equivalent to 19.14 cm^2. At a higher frequency (11.0 Hz) and a stroke amplitude of 40°, the required CF area is reduced to approximately $2.1A_1$, and the required torque decreases by 70.6% to 0.59 N.m (#2, Fig. 4A). For a stroke amplitude of 60° at 12.5 Hz, the same thrust production needs only a 76% smaller CF area (comparing A_2/A_1 = 1.2 and 5.0) and 86.1% less torque, with Q_2 being 0.28 N.m (compared with 2.01 N.m) (#3, Fig. 4A). For the tailbeat mechanism of KUFish-II, the DCX 22S-24V motor (Maxon, Switzerland, 66.0 grams, 10,800 RPM, 0.12 N.m stall torque) was chosen. Then, the available torques by a combination of motor-transmission systems can be calculated for the three GRs of 10.0, 14.0, and 18.0, using Eq. (7). The three parallel dashed lines on the two vertical principal planes in Fig. 4A represent the available torque. The results revealed that when the CF beats with a stroke

amplitude larger than approximately 30.0°, all three GRs satisfy the torque requirements. However, with the body length (L) and the assumed upper bound for the length of the CF ($L_c < 0.4\ L$), the tailbeat amplitude should be less than 60° to ensure a reasonable peak-to-peak amplitude ($A_m < 0.25\ L$). In addition, for efficient swimming at low St numbers, a relatively small A_m is suggested, which can be achieved by reducing the tailbeat amplitude. Accordingly, KUFish-II is designed with a GR of 18.0 and a stroke amplitude of 40° to create an A_m of approximately 0.25L (Step 2, Fig. 1).

Fig. 4B and C illustrate the comparison of the predicted frequency and required torque with the available values computed using Eqs. (6) and (7), respectively. The selected A_2/A_1 of 2.0 is expected to result in beating at the predicted frequency of 11.7 Hz (Fig. 4B), which is almost identical to the target frequency of 11.5 Hz (Step 1, Fig. 1). As the selected GR was 18.0, the available $f_{2,spec}$ computed using Eq. (6) was 10.0 Hz, which was 17% lower than 11.7 Hz. However, this 17% higher frequency can be achieved by applying a higher voltage than the motor's nominal voltage. The required torque computed using Eq. (5) is approximately 73% smaller than the available $Q_{2,spec}$ (comparing 0.57 and 2.16 N.m, respectively) (Fig. 4C). This ensures that the selected motor with a GR of 18.0 can provide sufficient torque and drive the tailbeat mechanism at 11.7 Hz. Thus, it is expected that a CF area double that of the KUFish ($2A_1$) can beat at 11.7 Hz, produce a thrust of 1.91 N, and achieve the target speed of 1.75 m/s.

3.2. Free-swimming undulatory kinematics

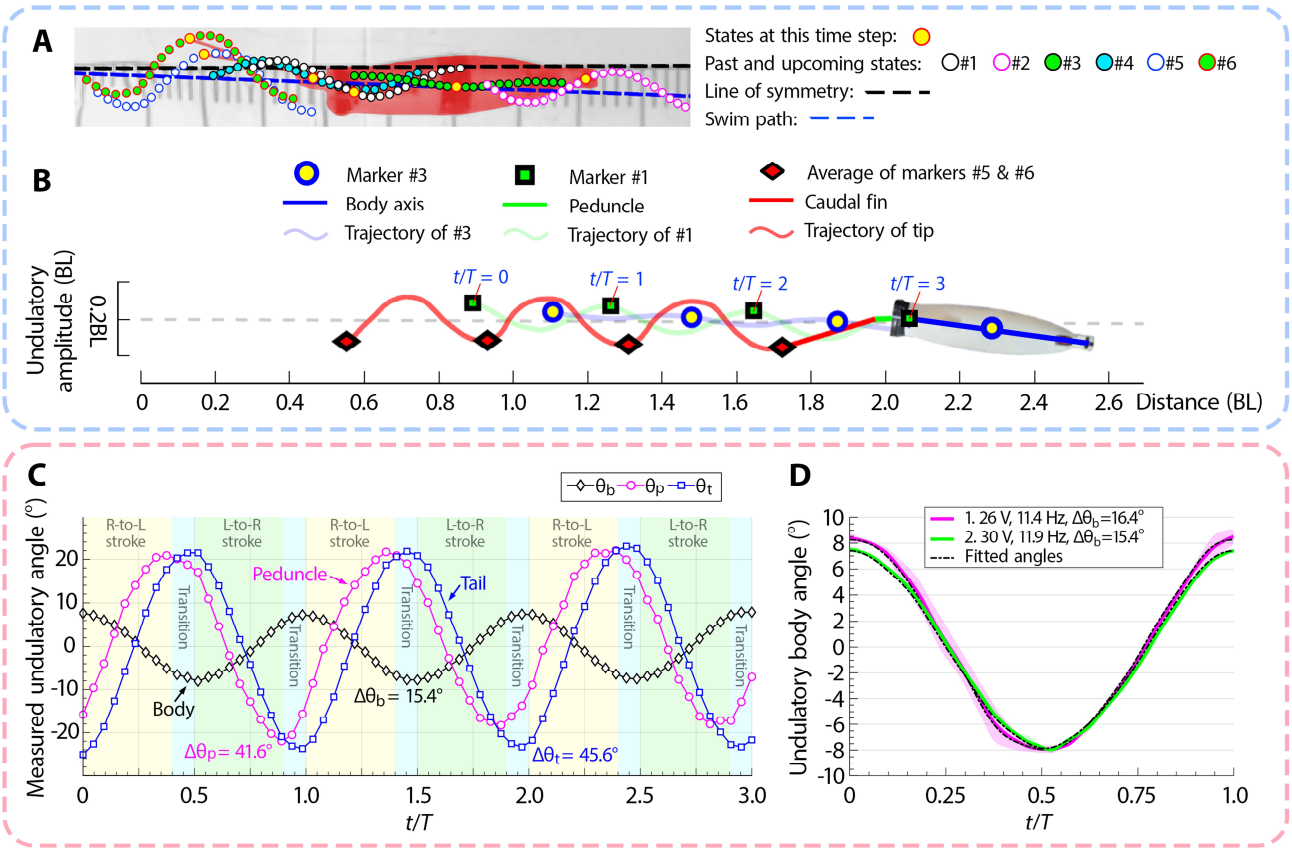

Fig. 5. Swimming kinematics. (**A**) Swimming trajectories of the six makers for the KUFish-II. (**B**) Reconstruction of two-dimensional (2D) pixel-based swim paths using MATLAB, based on the tracking data shown in (A). The horizontal grey dashed line represents the one-meter symmetry line of the pool, equivalent to 610 pixels or 2.7 BL. (**C**) Measured periodic undulatory angles for the body (θ_b), peduncle (θ_p), and CF (θ_t). (**D**) Measured and fitted body undulatory angles from two swimming tests powered by the 26-V and 30-V battery packages. The shaded zones represent the standard deviation. Marker numbering is detailed in Fig. 3C.

Fig. 5A shows the trajectories of the free-swimming KUFish-II, which is powered by an 8-cell battery package (150 mAh, 3.7 V, Lithium-Polymer, Dualsky, China), supplying an input of approximately 30 V. With this voltage application, the undulatory frequency was measured as 11.9 Hz for the body and 12.2 Hz for the CF. Thus, these frequencies are considered practically equivalent. In addition, the trajectory was considered nearly straight even without control, with a deviation of only 2.1° from the swimming direction (blue dashed lines in Fig. 5A).

Based on the tracking data in Fig. 5A and MATLAB analysis, Fig. 5B presents the pixel-based swim paths over three tailbeat cycles for the case with a maximum speed of 1.79 m/s. The corresponding swimming kinematics were processed and shown in Fig. 5C. Owing to the difficulty in maintaining swimming levels, the peaks of the measured undulatory angles increased. Therefore, the undulatory angle amplitudes were averaged over the first two cycles. The measured results show an amplitude of the peduncle angle of approximately 41.6° ($\Delta\theta_p$ in Fig. 5C), which is close to the designed tailbeat angle of 40.0°, thereby validating the design of the tailbeat mechanism. Due to tail flexibility, the tailbeat motion reaches a slightly larger amplitude of approximately 45.6° ($\Delta\theta_t$ in Fig. 5C). In contrast, the body undulates with a significantly smaller amplitude of about 15.4° ($\Delta\theta_b$ in Fig. 5C and D) and is completely out of phase with the tailbeat motion.

In addition to the 30-V case, the body undulation driven by a lower voltage battery package (26 V) was also examined (Fig. 5D). At 26 V, the body fairing undulates at 11.4 Hz, which is almost identical to the tailbeat frequency measured using the HSC. A comparison of the two voltage applications revealed that a 5.0% increase in frequency from 11.4 to 11.9 Hz reduces the body undulation angle by 6.0% from 16.4° to 15.4°. With differences in the frequency and undulation angle, defining the body drag coefficient is necessary to evaluate the swimming performance. Thus, the longitudinal force coefficients (C_{Fx}) were computed for the two cases shown in Fig. 5D using the CFD analysis, which were used to determine the body drag coefficient (C_D). In Appendix D, we explain how the body's undulatory motions were implemented in ANSYS Fluent (ANSYS Inc., Canonsburg, PA, USA).

3.3. Measured frequency, thrust, power, and free-swimming speed

Fig. 6A shows the measured thrust by the $2A_1$ CF at frequencies ranging from 8.0 to slightly over 12.0 Hz. To validate the reliability of the power measurements, we compared the independent thrust signals recorded during the thrust and power measurements (thrust shown in Fig. 6A and B, respectively; experimental setup shown in Fig. 3A). The comparison revealed a minor percentage difference in thrust between the two datasets. For example, in the thrust measurement (Fig. 6A), the interpolated thrust at the predicted tailbeat frequency of 11.7 Hz is 1.99 N. Meanwhile, in the power measurement, the interpolated thrust at the same frequency is 1.90 N (Fig. 6B). These measured values are within a 4% agreement with the prediction (1.91 N) by Eq. (2) at 11.7 Hz. This confirms the accuracy of the thrust measurement, thereby validating the power measurements for KUFish-II. The thrust values reported in this study were obtained from the thrust measurements in Fig. 6A.

The measured swimming speed and tailbeat frequency of the KUFish-II are summarized in Fig. 6C. The interpolated thrusts at two frequencies of 11.4 and 12.2 Hz, measured during free swimming at 26 V and 30 V, respectively (Fig. 6C), are shown in Fig. 6A as 1.92 N and 2.07 N. Despite meeting the thrust requirement of 1.91 N, KUFish-II with a 26 V input swam at 11.4 Hz, which is 3% lower than the predicted tailbeat frequency of 11.7 Hz (T = 1.92 N at 11.4 Hz; Fig. 6A). Therefore, its maximum swimming speed is only 1.56 m/s, resulting in an average of 1.52 ± 0.04 m/s (Fig. 6C). To slightly increase the tailbeat frequency, one more battery was added, forming a 30 V supply. This enabled the KUFish-II to increase the frequency from 11.4 to 12.2 Hz, produce 7.8% more thrust (2.07 N compared to 1.92 N, Fig. 6A), reach a maximum speed of 1.79 m/s, and maintain an average speed of 1.67 ± 0.04 m/s (Fig. 6C). Therefore, the robot with the $2A_1$ CF under 30 V meets the goal while consuming a power of 31.7 W (Fig. 6B). Additionally, the pixel-based measurement showed that the A_m was approximately 13.0% L (Fig. 5A and B). For validation, the calculated A_m using the measured maximum undulatory angles of the body, peduncle, and CF in Fig. 5C was also within 13%–14% L (see Fig. E1 and Appendix E for details). This revealed that KUFish-II swam at a St of 0.28, which is relatively smaller than those of the other robotic platforms (Fig. 6D). This value

also fell within the optimal range observed in nature (yellow shaded area in Fig. 6D). Thus, KUFish-II can be considered an efficient swimmer (Clapham and Hu, 2014; Iguchi et al., 2024; Wen et al., 2013; White et al., 2021; Zhong et al., 2017; Zhu et al., 2019).

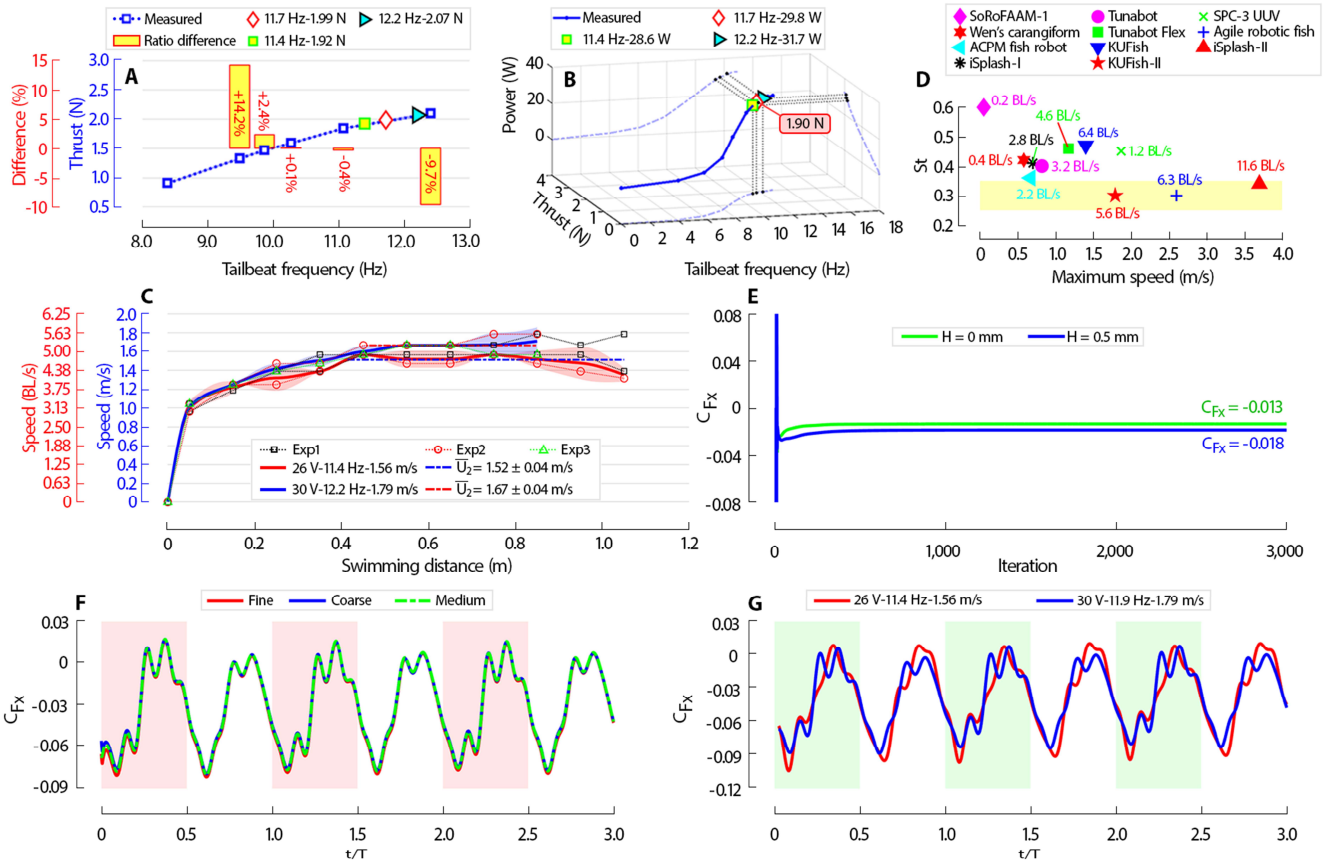

Fig. 6 Experimental and CFD results. (**A-D**) Experimental results of (A) cycle-average thrust by the $2A_1$ CF across varying tailbeat frequencies (shaded areas show standard deviation from three trials, 95.0% confidence level), (B) averaged measured power consumption versus tailbeat frequency, alongside corresponding thrust production, (C) swimming speeds of 26-V and 30-V KUFish-II (shaded regions indicate standard deviation from two trials for 26-V cases, and three trials for 30-V cases, 95.0% confidence level), and (D) comparison of St and maximum speeds for KUFish-II and other robots with the shaded region showing $0.25 < St < 0.35$. See Movies S2 to S8 for tethered and free-swimming tests. (**E-G**) CFD results: (E) Body drag coefficient during steady, static swimming. (F) Mesh convergence study of C_{Fx} for zero-roughness model undulating at 11.9 Hz (30 V) across three mesh types, using the corresponding measured undulatory kinematics in Fig. 5D. (G) Time courses of C_{Fx} for two models at the body undulatory frequencies of 11.4 Hz (26 V) and 11.9 Hz (30 V), based on their respective measured kinematics shown in Fig. 5D. Note: roughness height is 0 mm in (F) and 0.5 mm in (G). See Appendix D and Fig. D1 for more details of the CFD modeling and analysis.

Although the swimming speed primarily depends on the thrust produced by the CF, minimizing body drag is also a critical factor in enhancing the swimming performance (Webb, 1988). Therefore, estimating body drag during undulatory swimming is essential to complete the design process. Using CFD analysis based on the measured body undulatory kinematics, the body drag coefficient of KUFish-II was numerically determined. In the CFD analysis, we applied the same meshing technology used to describe the dynamic mesh motions of the flapping wing and tailbeat motion (Nguyen et al., 2024, 2022, 2021b, 2021a; Nguyen and Park, 2023). Here, Fig. 6E-G and Table 1 summarize the CFD results on the effects of undulatory frequency on longitudinal force production along the body's x-axis. A negative cycle-average C_{Fx} indicates the body drag, whereas a positive value denotes the thrust. Therefore, the drag coefficient is equivalent to the absolute value of C_{Fx} in Table 1.

Table 1. Cycle-average body drag coefficient

Voltage (V)	f_b (Hz)	$\Delta\theta_b$ (°)	C_{Fx} (H = 0 mm)	C_{Fx} (H = 0.5 mm)	$C_D = \lvert C_{Fx} \rvert$
26	11.4	16.4	N/A	-0.037	0.037
30	11.9 (+4.4%)	15.4 (-6.1%)	-0.029	-0.035 (-5.4%)	0.035

A mesh convergence study using the zero-roughness model across three different mesh types is shown in Fig. 6F, demonstrating that the results obtained with the medium mesh converged at the third cycle. Table 1 compares the cycle-average C_{Fx} by 26-V and 30-V inputs, corresponding to the body undulatory frequencies of 11.4 and 11.9 Hz, respectively. The results showed that a 4.4% increase in undulatory frequency led to a 6.1% decrease in the body's undulatory angle, which in turn resulted in a 5.4% reduction in the total C_{Fx}. Interpretations of the relationship among swimming speed, body undulatory angle, and body drag coefficient are detailed in Section 4. Notably, the C_{Fx} value of -0.035 (H = 0.5 mm, Table 1) obtained by 30-V undulatory swimming was approximately double that of -0.018 computed from the static swimming simulation (see H = 0.5 mm, Fig. 6E). This trend is similar to previous findings reported for the body shape of KUFish (Nguyen et al., 2022).

4. Discussion

The measured frequency, thrust, and swimming speed were consistent with the predicted values. Therefore, the current scaling-based design can provide the key specifications for motor selection. With a properly selected motor and GR, the fabricated tailbeat mechanism produced the required thrust by beating the CF with the predicted area and frequency. Thus, the scaling-based design proposed in this paper may provide a systematic design methodology for robotic fish. The swimming speed predicted by the three physical parameters is a good estimation for the target speed. At the tailbeat frequency of 12.2 Hz, the KUFish-II swam mostly straight even without feedback control, generated a thrust of approximately 2.1 N, and reached a maximum speed of 1.79 m/s. In addition, the robot achieved a maximum Fr of 1.01 and a Reynolds number on the order of 10^5 (see Section D.1), consistent with high-burst swimming regime at 1.79 m/s (5.6 BL/s) (Bandyopadhyay, 2005). The swimming speed prediction using three physical parameters indicates that the body length must be longer to swim faster than 1.79 m/s.

With the tethered measurement, we compared the scaling ratios of the thrust with those of the square of the tailbeat frequency to investigate the accuracy of the thrust measurement using Eq. (3) for the same θ and A. The differences between the ratios of $(T_{i\text{-th}}/T_{(i-1)\text{-th}})$ and $(f_{i\text{-th}}/f_{(i-1)\text{-th}})^2$ measured at two consecutive frequencies are indicated by yellow columns (Fig. 6A). For the measured frequencies of 9.9, 10.3, and 11.1 Hz, which are close to the predicted frequency of 11.0 Hz, the ratio differences are less than 2.4%. This indicates that the thrusts at these frequencies were accurately measured. However, the differences are 14.2% for frequencies between 8.4 and 9.5 Hz and -9.7% for frequencies between 11.1 and 12.4 Hz. The relatively large ratio difference of 14.2% is mainly due to the difficulty in accurately measuring the thrust at low frequencies, where the undulatory motion of the robot was not well bounded during the left and right tailbeat motions. At a higher frequency (12.4 Hz), the CF deformed more because of faster motion, which made the thrust nonproportional to the square of the frequency. Thus, the negative difference of -9.7% is subsequently attributed to larger bending of the CF. Consequently, although the scaling-based thrust prediction is reliable near the design frequency, its accuracy cannot be guaranteed at frequencies significantly above or below the design frequency, revealing the limitations of the method. In addition, since the CF thickness of 0.6 mm was chosen by trial and error, the influence of CF stiffness on thrust should be somehow included in the scaling method. Previous work (Prempraneerach et al., 2003) also showed that an optimally flexible foil improved efficiency by 38%, while its thrust remained nearly unchanged. This indicates the need to account for tail flexibility in the scaling (Triantafyllou et al., 2005).

The measured swimming kinematics indicated that KUFish-II swam efficiently with a St of approximately 0.28, falling within the optimal range of 0.25 to 0.35 for natural species. Similar conclusions were drawn from studies on oscillating airfoils (Anderson et al., 1998; Lauder and Tytell, 2005; Read et al., 2003; Triantafyllou et al., 1991; Wen et al., 2013). In fact, the propulsive efficiency dropped significantly within the range of $0.35 < St < 1.025$ after

peaking at St = 0.3125 (Wen et al., 2013). Similarly, the authors of (Read et al., 2003) tested St outside the optimal range to compare the thrust coefficient and propulsive efficiency of underwater oscillating foils. The results showed a slight decrease in the thrust coefficient (0.62 vs. 0.58) and a 20% drop in efficiency (60% vs. 40%) as St increased from 0.4 to 0.6, indicating that both were caused by the transition from thrust to drag. By comparison, the original KUFish swam at a speed of 1.40 m/s with a St of 0.45, whereas the KUFish-II achieved a faster speed of 1.79 m/s with a 37.8% lower St of 0.28. This shows that the swimming speed increase from 1.40 to 1.79 m/s is associated with a decrease in St from 0.45 to 0.28. A similar trend in the relationship between swimming speed and St was also observed in real fish (Lauder and Tytell, 2005) and further validated using the Tunabot robotic platform (Zhu et al., 2019). Although a higher St results in an increase in thrust, it may produce significant drag, causing a slowdown in swimming speed (Read et al., 2003; Wen et al., 2013).

Additionally, at 12.2 Hz, the KUFish-II consumed 31.7 W to reach 1.79 m/s (5.6 BL/s), which corresponds to a cost of transport (COT) equal to 17.7 J/m, defined as the ratio of power consumption to swimming speed (Lauder et al., 2012; Tangorra et al., 2011; Zhu et al., 2019). The COT of KUFish-II is only 17% of that of the 1.6-m-long SPC-3 UUV (Wang et al., 2010), which swam at a similar speed of 1.87 m/s (1.2 BL/s) but consumed approximately 190.0 W, resulting in a COT of 101.6 J/m. Compared with the robots of similar body lengths but faster swimming speeds, KUFish-II still requires 45% and 72% less energy to swim over one meter than the 0.32-m-long iSplash-II, with a COT of 32.4 J/m, consuming 120.0 W at 3.7 m/s (11.6 BL/s) (Clapham and Hu, 2015), and the 0.41-m-long agile robotic fish, with a COT of 65.4 J/m, consuming ~ 170 W at 2.6 m/s (6.3 BL/s) (Iguchi et al., 2024), respectively.

The CFD analysis revealed that the rightward body undulation shifts the stagnation point and high-pressure region at the nose to the right (highlighted in red; see Step 6, Fig. 1). Simultaneously, the low-pressure region (blue) on the left side moves anteriorly, creating a pressure difference across the nose. This subsequently causes water to flow from the high-pressure to low-pressure side, generating a leftward force owing to the leading-edge suction from the airfoil-like shape of the anterior body (Step 6, Fig. 1). See Movie S9 for details. This phenomenon aligns with the findings of a previous study (Lucas et al., 2020) on thrust generation in the negative pressure region of the anterior airfoil-like body. The resulting force also helps reduce the undulatory body angle by generating a counterclockwise restoring moment about the center of buoyancy (CB). As the robot swims faster, a greater leftward force is produced during the rightward undulation owing to the increased inflow speed relative to the body (Step 6, Fig. 1). A similar mechanism occurs during leftward undulation, when a rightward force and an associated clockwise restoring moment are produced. This explains why the KUFish-II exhibited smaller body undulation at higher swimming speeds (15.4° at 30 V, 1.79 m/s) than at slower speeds (16.4° at 26 V, 1.56 m/s) (Table 1). The reduced undulatory angle subsequently decreased the frontal area, thereby lowering the body drag ($C_D = 0.037$ by 0.035, Table 1).

Using Eq. (1), for the wetted body area of 0.0262 m^2, the computed C_D of approximately 0.04 (Table 1), and the average measured thrust of 2.07 N at 12.2 Hz, the robot is estimated to reach the maximum speed of 1.96 m/s (9.3% higher than the measured speed of 1.79 m/s) after swimming a distance of 0.55 m. Therefore, the focal area from 0.6 to 1.0 m is sufficient for accurate speed measurement, even though the 1D equation overestimates the maximum speed compared with the measured data. This indicates that the actual C_D may exceed 0.04 owing to a slight pitching motion during swimming, as evidenced by fluctuations in the measured swimming speeds (Fig. 6C).

5. Conclusion

This study successfully introduced a scaling-based design approach for an energy-efficient, fish-inspired tailbeat robot capable of achieving a target high swimming speed characterized by a Froude number of 1.0. Together with the Strouhal number and reduced frequency, the target swimming speed of the 0.32-m-long KUFish-II was estimated at 1.75 m/s (5.5 BL/s). Upon fabrication and testing, the robot achieved a swimming speed of 1.79 m/s (5.6 BL/s) with a tailbeat frequency of 12.20 Hz. The swimming required a power of 31.7 W, resulting in a cost of transport of 17.7 J/W, which is significantly lower than that of robots operating at comparable speeds. Notably, the tailbeat stroke angle of 40° was systematically designed to minimize unwanted body undulation, leading to a measured peak-to-peak amplitude of about 13% of the body length. Consequently, the robot swam with a St of 0.28, which lies within the observed range for high propulsive efficiency in natural species. These results demonstrate the effectiveness and

applicability of the proposed scaling-based design approach to the development of efficient and scalable tailbeat swimming robots.

Appendix A: Tables

Table A1. Comparison between the predicted and actual (measured) values of three physical parameters and their corresponding swimming speeds

Parameters	Units	Predicted	Actual	Difference
Total length	m	0.32	0.32	
Wake width/total length	%	20.00	13.00	-35.0%
Target tailbeat frequency	Hz	11.50	12.20	6.1%
Froude number	-	1.00	1.01	1.0%
Strouhal number	-	0.42	0.28	-32.6%
Reduced frequency	-	13.30	13.70	3.0%
U by Fr	m/s	1.77	1.79	1.0%
U by St	m/s	1.75	1.79	2.3%
U by sigma	m/s	1.74	1.79	3.0%
Average possible swimming speed	m/s	1.75	1.79	2.1%

Table A2. Actual parameters of KUFish and estimated ones of KUFish-II

Parameters	Symbols	KUFish (Pham et al., 2023)	KUFish-II	Units
Body length	L	0.22	0.32	m
Length of CF	L_C	0.06 (= 27% L)	< 40% L = 0.12	m
Total mass	M	$M_1 = 0.116$	$M_2 = 1.2 \times M_1 = 0.139$	kg
Motor mass	M_m	$M_{m1} = 0.025$	$M_{m2} = 0.066$	kg
Body volume	V	$V_1 = 0.000116$	$V_2 = 1.2 \times V_1 = 0.000139$	m^3
Body wetted area	S	$S_1 = 0.0211$	$S_2 = (1.2)^{2/3} \times S_1 = 0.0238$	m^2
Swimming speed	U	1.40	1.75	$m.s^{-1}$
Tailbeat frequency	f	11.4	11.7	Hz
Thrust	T	1.08	1.91	N
Area of CF	A	$A_1 = 1.914 \times 10^{-3}$	$A_2 = 2.0 \times A_1$	m^2
Fin span	b	0.07	0.1	m
Aspect ratio	AR	2.56	2.56	
Required torque	Q	0.144	0.57	N.m
Reduction gear ratio	GR	14.4	18.0	

Appendix B: Updates for the scaling-based equations of predicted thrust and torque

Table B1 summarizes the data used to derive Eq. (3). These data, which were obtained in (Nguyen et al., 2023), were extracted from a series of CFD analyses using ANSYS Fluent. More details on the CFD modeling and simulation can be found in (Nguyen et al., 2023). More specifically, using the relationships between $T \sim (A^2$ and $\omega^2)$ and $Q \sim (A^{2.5}$ and $\omega^2)$, as presented in (Nguyen et al., 2023), Eqs. (B1) and (B2) describe the ratios of thrust (T_2/T_1) and torque (Q_2/Q_1) for the caudal fin areas (A_2/A_1) and tailbeat frequencies (f_2/f_1), where subscripts "1" and "2" denote the two different cases being investigated.

$$\frac{T_2}{T_1} = \left(\frac{A_2}{A_1}\right)^2 \times \left(\frac{f_2}{f_1}\right)^2. \quad \text{(B1)}$$

$$\frac{Q_2}{Q_1} = \left(\frac{A_2}{A_1}\right)^{2.5} \times \left(\frac{f_2}{f_1}\right)^2 . \quad \text{(B2)}$$

Table B1. Cycle-average thrust by the CFD simulations and exponent "x" values

Tailbeat frequency (Hz)		10			20			30		
Tailbeat stroke amplitude (°)		20	50	80	20	50	80	20	50	80
Thrust by different ratios of CF areas (N)	1.0	0.1	0.9	2.3	0.4	3.6	9.0	1.0	8.0	20.3
	2.25	0.5	4.5	11.3	2.2	18.0	45.3	4.8	40.5	101.9
	4.0	1.8	14.3	36.4	7.1	57.3	145.7	15.9	128.9	327.9
Ratios of stroke amplitude			50/20	80/50		50/20	80/50		50/20	80/50
Exponent "x" by different ratios of CF areas	1.0		2.40	2.00		2.40	1.95		2.27	1.98
	2.25		2.40	1.96		2.29	1.96		2.33	1.96
	4.0		2.26	1.99		2.28	1.99		2.28	1.99
Average "x"		2.15								

However, the relationship between thrust and torque with respect to stroke amplitude has not yet been established in (Nguyen et al., 2023). For the same tail area $(A_2 = A_1)$ and frequency $(f_2 = f_1)$, the ratios of thrust, and torque are assumed to be proportional to the x^{th} and y^{th} powers of the change in stroke amplitude, respectively, as follows:

$$\frac{T_2}{T_1} = \left(\frac{\theta_2}{\theta_1}\right)^x \text{ and } \frac{Q_2}{Q_1} = \left(\frac{\theta_2}{\theta_1}\right)^y . \quad \text{(B3)}$$

Then, the unknown exponents "x" and "y" are computed using Eq. (B4).

$$x = \log\left(\frac{T_2}{T_1}\right)/\log\left(\frac{\theta_2}{\theta_1}\right) \text{ and } y = \log\left(\frac{Q_2}{Q_1}\right)/\log\left(\frac{\theta_2}{\theta_1}\right). \quad \text{(B4)}$$

To determine the unknown exponent "x", we use the CFD results in Table B1. Specifically, at different tailbeat frequencies, we calculated the ratios of the thrust produced by different stroke amplitudes, along with their corresponding stroke amplitude ratios. The exponent "x" was computed using the logarithmic relationship in Eq. (B4). Table B1 summarizes the computed "x" values, with an average of 2.15. Then, by accounting for the stroke amplitude, the relationship among the thrust, CF area, and tailbeat frequency in Eq. (B1) was then updated as follows:

$$\frac{T_2}{T_1} = \left(\frac{A_2}{A_1}\right)^2 \times \left(\frac{f_2}{f_1}\right)^2 \times \left(\frac{\theta_2}{\theta_1}\right)^{2.15} . \quad \text{(B5)}$$

Table B2. Peak torque values for the CF of KUFish-II and the corresponding "y" values across three tailbeat frequencies and amplitudes

Tailbeat frequency (Hz)	10			20			30		
Tailbeat stroke amplitude (°)	20	50	80	20	50	80	20	50	80
Peak torque (Nm)	0.4	1.0	1.6	1.6	4.0	6.5	3.6	9.1	14.5
Exponent "y"	1.00	1.00		1.00	1.00		1.00	1.00	
Average "y"	1.00								

To determine the unknown exponent "y" in Eq. (B4), we employed the added mass method described in (Pham et al., 2023) to compute the peak torques generated by the $2A_1$ CF of the KUFish-II for three stroke amplitudes of (20°, 50°, and 80°) and the tailbeat frequencies of (10, 20, and 30) Hz (see Table B2). By calculating the torque ratio corresponding to the change in stroke amplitude, the exponent "y" is shown in Table B2, with an average of 1.0.

Finally, by incorporating the stroke amplitude, the relationship among the torques, tail fin areas, and tailbeat frequencies in Eq. (B2) is then updated as follows:

$$\frac{Q_2}{Q_1}=\left(\frac{A_2}{A_1}\right)^{2.5}\times\left(\frac{f_2}{f_1}\right)^{2.0}\times\left(\frac{\theta_2}{\theta_1}\right). \tag{B6}$$

Appendix C: Fourier functions used to fit measured undulatory kinematics

The measured undulatory kinematics in Fig. 5D were fitted using the Fourier functions as follows:

$$f(\hat{t})=a_0+\sum_{k=1}^{n=9}\left[a_k\cos(2k\pi f(\hat{t}+\hat{t}_s))+b_k\sin(2k\pi f(\hat{t}+\hat{t}_s))\right], \tag{C1}$$

where the fitting coefficients a_0, a_k, and b_k were incorporated into a user-defined function (UDF) in ANSYS Fluent to implement the prescribed kinematics. Here, $\hat{t}$ shows the nondimensional time (t/T), and $\hat{t}_s = 0.25$ denotes the phase shift at which the body axis is close to the swimming axis, ensuring mesh symmetry for each half-stroke.

Appendix D: CFD modeling and analysis

D.1. CFD modeling

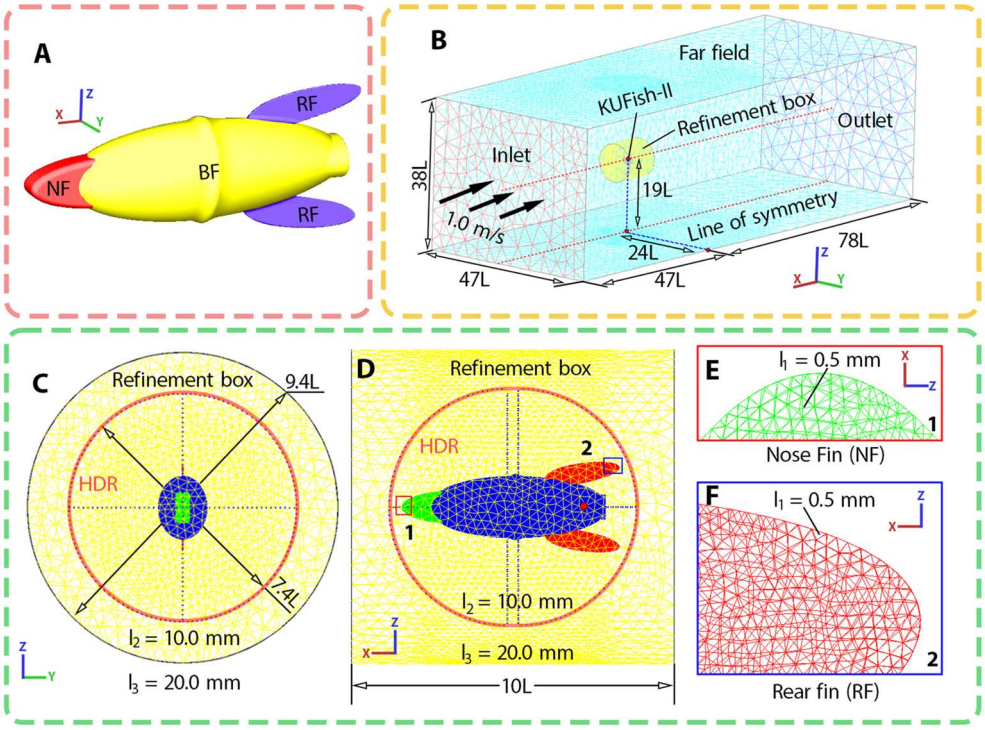

Fig. D1. CFD modeling. (**A**) Outer shape of the robot. (**B-F**) Mesh configurations, including (B) full computational domain; (C) front and (D) side views of the refinement boxes around the body with high-density regions (HDRs); (E) close-up view of the surface mesh at the nose fin and (F) at the RF.

In Fig. D1, the body was positioned at the center of the longitudinal plane of symmetry, with its origin aligned to the tailbeat rotation axis (Fig. 2B). Three parameters including l_1, l_2, and l_3 (see Figs. D1C-F), were used to create the mesh, where l_1 is the maximum edge length of the triangular elements on the body surface, l_2 is the maximum edge length of the tetrahedral cells within the HDR, and l_3 is the maximum edge length of the triangular elements at the boundary of the refinement box. Similar to our previous CFD studies on periodic motion (Nguyen et al., 2024, 2022, 2021b, 2021a; Nguyen and Park, 2023), the time step was set to 0.1% of the undulatory frequency of the body. To model the flow characteristics over the body, while accounting for surface roughness, the k–ε two-

equation turbulent model was employed, as it effectively captures the convection and diffusion of turbulent energy. This model is particularly suitable for the flow regimes with the high Re values of 4.8×10^5 for 26-V and 5.3×10^5 for 30-V swimming, which are calculated as follows:

$$\mathrm{Re} = \frac{\bar{U}_2 \times L}{\nu}, \tag{D1}$$

where ν is the water kinematic viscosity at 20 °C (1.004×10^{-6} m^2/s), $\bar{U}_2$ represents the averaged swimming speeds of 1.67 m/s at 30 V and 1.56 m/s at 26V.

D.2. Convergence criteria

The CFD convergence was achieved with residual errors of the order of 10^{-6} for the continuity equation and the k–ε turbulence model, and 10^{-9} for the velocity components. This ensured that the solutions converged with insignificant changes between successive iterations during steady swimming. Similar convergence criteria were obtained for the undulatory swimming simulations. At each timestep, the results reached residuals of 10^{-6} and 10^{-9}, corresponding to the continuity equation and k–ε turbulence model, and the velocity components, respectively.

D.3. Definition of the longitudinal force coefficient

The coefficient of longitudinal force along the x-axis, C_{Fx} is computed as follows:

$$C_{Fx} = \frac{2 \times F_x}{\rho \times S \times \bar{U}_{2'}^2}, \tag{D2}$$

where F_x is the cycle-average force on the x-axis computed using CFD, and $\bar{U}_{2'}$ is the reference speed of 1.0 m/s.

D.4. Effects of surface roughness on C_{Fx} during undulatory swimming

The effects of surface roughness were investigated by comparing the C_{Fx} produced from two CFD models: one with zero roughness (H = 0 mm) and one with 0.5-mm roughness (H = 0.5 mm). The converged C_{Fx} of -0.013 for the zero-roughness model and -0.018 for the 0.5-mm roughness model indicate a 38% increase in drag after 3,000 iterations, as shown in Fig. 6E for the static and steady swimming.

D.5. Mesh convergence study for the simulation of static swimming

A mesh convergence study was conducted on a zero-roughness model over three-body undulatory cycles. The results from the third cycle showed nearly identical values of the cycle-averaged C_{Fx} across the three mesh types: $C_{Fx} = -0.029$ for both coarse and medium meshes and $C_{Fx} = -0.030$ for the fine mesh. Thus, the mesh was considered to converge for the zero-roughness model and was assumed to be sufficiently accurate for simulations with a roughness height of 0.5 mm as well.

Appendix E: Comparison between the actual swimming speed and three predicted values

Table A1 compares the average predicted swimming speed with the measured value of 1.79 m/s. Due to a 6% higher tailbeat frequency (12.2 Hz versus 11.5 Hz), the measured swimming speed was approximately 2.1% higher than the predicted value of 1.75 m/s. In addition, three actual physical parameters of Fr, St, and σ were compared with their predicted counterparts (see Table A1). The results showed that the actual Fr (1.01) was nearly identical to its prediction (1.00), while the actual σ (13.70) slightly differed by 3% from the predicted value (13.30).

However, a 35% decrease in the actual A_m (13% L) compared to its predicted value (20% L) was the primary result of the 33% discrepancy between the actual St (0.28) and its predicted value (0.42) (Table A1). The actual A_m

was measured using 2D-pixel-based coordinates extracted from the video. For validation, the peak-to-peak distance were also computed using the measured amplitudes of the undulatory angles of the body, peduncle, and CF (as shown in Fig. 5C). The computed A_m was also approximately 13–14% L, closely matching the pixel-based measurement (Fig. E1). Thus, properly estimating A_m is important for the initial prediction of the target swimming speed.

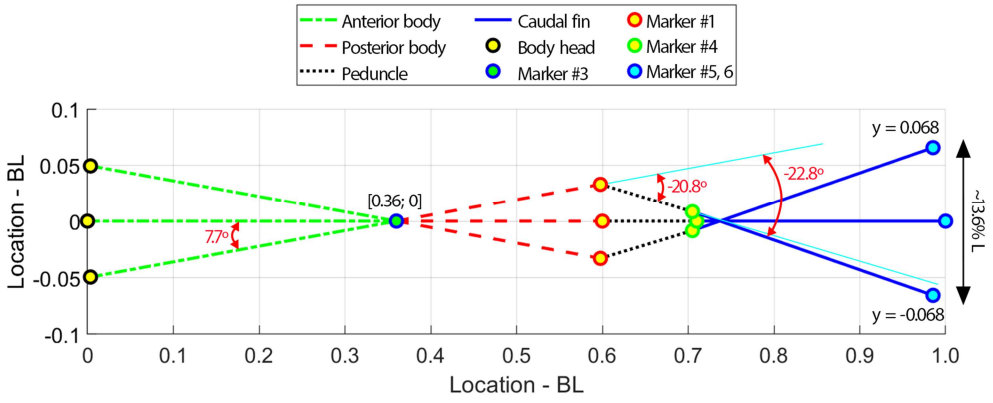

Fig. E1. Validation of the measured pixel-based peak-to-peak amplitude. Since the phase of body undulation was opposite to those of the peduncle and CF, the calculation used the maximum undulatory angles for body ($\pm$ 7.7°), peduncle ($\mp$20.8°), and CF ($\mp$22.8°), as shown in Fig. 5C. Notably, the undulatory frequencies of the body, peduncle, and CF were assumed to be identical.

Acknowledgment

We thank H.V. Phan for helpful comments and suggestions on the manuscript, and G. Ha, P. H. Hoang, and T. H. Pham for their valuable discussions, assistance with software installation, and guidance on experimental equipment use. **Funding:** This study was supported by the Korea Research Institute for Defense Technology Planning and Advancement (KRIT) grant funded by the Korean government (Defense Acquisition Program Administration, DAPA) under project number KRIT-CT-23-008: Development of a biomimetic underwater robot platform, 2023. **Author contribution:** All the authors reviewed and revised the manuscript. **KN** provided a strategy for selecting the design parameters for swimming speed estimation using physical parameters, updated the esquations, developed a program for the scaling-based design approach for detailed estimations, designed and fabricated the KUFish-II platform, planned and designed the experiments, performed all the measurements and simulations, analyzed the data, interpreted and validated all the results, created the figures, and drafted the original manuscript. **HCP** suggested the use of physical parameters in swimming speed prediction, formulated original equations for the scaling-based design, developed the added mass method and 1D equation, searched for potential motors, prepared the experimental space, supervised the project, validated the results, and provided resources.

References

Anderson, J.M., Chhabra, N.K., 2002. Maneuvering and stability performance of a robotic tuna. Integr Comp Biol 42, 118–126. https://doi.org/10.1093/icb/42.1.118

Anderson, J.M., Streitlien, K., Barrett, D.S., Triantafyllou, M.S., 1998. Oscillating foils of high propulsive efficiency. J Fluid Mech 360, 41–72. https://doi.org/10.1017/S0022112097008392

Aureli, M., Kopman, V., Porfiri, M., 2010. Free-Locomotion of Underwater Vehicles Actuated by Ionic Polymer Metal Composites. IEEE/ASME Transactions on Mechatronics 15, 603–614. https://doi.org/10.1109/TMECH.2009.2030887

Bainbridge, R., 1958. The Speed of Swimming of Fish as Related to Sisze and to the Frequency and Amplitude of the Tail Beat. Journal of Experimental Biology 35, 109–133. https://doi.org/10.1242/jeb.35.1.109

Bandyopadhyay, P.R., 2005. Trends in biorobotic autonomous undersea vehicles. IEEE Journal of Oceanic Engineering 30, 109–139. https://doi.org/10.1109/JOE.2005.843748

Bandyopadhyay, P.R., 2002. Maneuvering Hydrodynamics of Fish and Small Underwater Vehicles. Integr Comp Biol 42, 102–117. https://doi.org/10.1093/icb/42.1.102

Barrett, D.S., 1996. Propulsive efficiency of a flexible hull underwater vehicle (Doctoral dissertation). Massachusetts Institute of Technology.

Bartol, I.K., Gharib, M., Weihs, D., Webb, P.W., Hove, J.R., Gordon, M.S., 2003. Hydrodynamic stability of swimming in ostraciid fishes: role of the carapace in the smooth trunkfish *Lactophrys triqueter* (Teleostei:Ostraciidae). Journal of Experimental Biology 206, 725–744. https://doi.org/10.1242/jeb.00137

Belmonte, A., Eisenberg, H., Moses, E., 1998. From Flutter to Tumble: Inertial Drag and Froude Similarity in Falling Paper. Phys Rev Lett 81, 345–348. https://doi.org/10.1103/PhysRevLett.81.345

Breder, C.M., 1926. The locomotion of fishes. Zoologica 4, 159–297.

Clapham, R.J., Hu, H., 2015. iSplash: Realizing Fast Carangiform Swimming to Outperform a Real Fish, in: Robot Fish. Springer, Berlin, Heidelberg, pp. 193–218. https://doi.org/10.1007/978-3-662-46870-8_7

Clapham, R.J., Hu, H., 2014. iSplash-I: High performance swimming motion of a carangiform robotic fish with full-body coordination, in: 2014 IEEE International Conference on Robotics and Automation (ICRA). IEEE, pp. 322–327. https://doi.org/10.1109/ICRA.2014.6906629

Dean, B., Bhushan, B., 2010. Shark-skin surfaces for fluid-drag reduction in turbulent flow: a review. Philosophical Transactions of the Royal Society A: Mathematical, Physical and Engineering Sciences 368, 4775–4806. https://doi.org/10.1098/rsta.2010.0201

Driscoll, F.R., Alsenas, G.M., Beaujean, P.P., Ravenna, S., Raveling, J., Busold, E., Slezycki, C., 2008. A 20 KW open ocean current test turbine, in: OCEANS 2008. IEEE, pp. 1–6. https://doi.org/10.1109/OCEANS.2008.5152104

Drucker, E.G., Lauder, G. V., 2001. Locomotor function of the dorsal fin in teleost fishes: experimental analysis of wake forces in sunfish. Journal of Experimental Biology 204, 2943–2958. https://doi.org/10.1242/jeb.204.17.2943

Eloy, C., 2012. Optimal Strouhal number for swimming animals. J Fluids Struct 30, 205–218. https://doi.org/10.1016/j.jfluidstructs.2012.02.008

Floryan, D., Van Buren, T., Rowley, C.W., Smits, A.J., 2017. Scaling the propulsive performance of heaving and pitching foils. J Fluid Mech 822, 386–397. https://doi.org/10.1017/jfm.2017.302

Floryan, D., Van Buren, T., Smits, A.J., 2018. Efficient cruising for swimming and flying animals is dictated by fluid drag. Proceedings of the National Academy of Sciences 115, 8116–8118. https://doi.org/10.1073/pnas.1805941115

Han, P., Lauder, G. V., Dong, H., 2020. Hydrodynamics of median-fin interactions in fish-like locomotion: Effects of fin shape and movement. Physics of Fluids 32, 011902. https://doi.org/10.1063/1.5129274

Hedrick, T.L., 2008. Software techniques for two- and three-dimensional kinematic measurements of biological and biomimetic systems. Bioinspir Biomim 3, 034001. https://doi.org/10.1088/1748-3182/3/3/034001

Hu, Y., Liang, J., Wang, T., 2015. Mechatronic design and locomotion control of a robotic thunniform swimmer for fast cruising. Bioinspir Biomim 10, 026006. https://doi.org/10.1088/1748-3190/10/2/026006

Iguchi, K., Shimooka, T., Uchikai, S., Konno, Y., Tanaka, H., Ikemoto, Y., Shintake, J., 2024. Agile robotic fish based on direct drive of continuum body. npj Robotics 2, 7. https://doi.org/10.1038/s44182-024-00014-z

Jaya, A.S., Kartidjo, M.W., 2022. Thrust and efficiency enhancement scheme of the fin propulsion of the biomimetic Autonomous Underwater Vehicle model in low-speed flow regime. Ocean Engineering 243, 110090. https://doi.org/10.1016/j.oceaneng.2021.110090

Lauder, G.V., Tytell, E.D., 2005. Hydrodynamics of Undulatory Propulsion. Fish physiology 23, 425–468. https://doi.org/10.1016/S1546-5098(05)23011-X

Lauder, G. V., Flammang, B., Alben, S., 2012. Passive Robotic Models of Propulsion by the Bodies and Caudal Fins of Fish. Integr Comp Biol 52, 576–587. https://doi.org/10.1093/icb/ics096

Lindsey, C.C., 1978. Form, Function, and Locomotory Habits in Fish. Fish Physiology 7, 1–100. https://doi.org/10.1016/S1546-5098(08)60163-6

Liu, G., Ren, Y., Dong, H., Akanyeti, O., Liao, J.C., Lauder, G. V., 2017. Computational analysis of vortex dynamics and performance enhancement due to body–fin and fin–fin interactions in fish-like locomotion. J Fluid Mech 829, 65–88. https://doi.org/10.1017/jfm.2017.533

Lucas, K.N., Lauder, G. V., Tytell, E.D., 2020. Airfoil-like mechanics generate thrust on the anterior body of swimming fishes. Proceedings of the National Academy of Sciences 117, 10585–10592. https://doi.org/10.1073/pnas.1919055117

Matta, A., Pendar, H., Battaglia, F., Bayandor, J., 2020. Impact of caudal fin shape on thrust production of a thunniform swimmer. J Bionic Eng 17, 254–269. https://doi.org/10.1007/s42235-020-0020-9

Nguyen, K., Au, L.T.K., Phan, H.-V., Park, H.C., 2021a. Comparative dynamic flight stability of insect-inspired flapping-wing micro air vehicles in hover: Longitudinal and lateral motions. Aerosp Sci Technol 119, 107085. https://doi.org/10.1016/j.ast.2021.107085

Nguyen, K., Au, L.T.K., Phan, H.-V., Park, S.H., Park, H.C., 2021b. Effects of wing kinematics, corrugation, and clap-and-fling on aerodynamic efficiency of a hovering insect-inspired flapping-wing micro air vehicle. Aerosp Sci Technol 118, 106990. https://doi.org/10.1016/j.ast.2021.106990

Nguyen, K., Ha, G., Kang, T., Park, H.C., 2024. Analysis of hovering flight stability of an insect-like flapping-wing robot in Martian condition. Aerosp Sci Technol 152, 109371. https://doi.org/10.1016/j.ast.2024.109371

Nguyen, K., Ha, G., Park, H.C., 2023. Preliminary design of a fish-like fast-swimming robot by scaling of the KUFish, in: The 19th International Conference on Intelligent Unmanned Systems. Adelaide, Australia.

Nguyen, K., Park, H.C., 2023. Feasibility study on mimicking the tail-beating supported gliding flight of flying fish. Ocean Engineering 287, 115745. https://doi.org/10.1016/j.oceaneng.2023.115745

Nguyen, K., Pham, T.H., Park, H.C., 2022. Numerical investigation of hydrodynamics for a fish-like robot under undulatory forward swimming, in: Annual Meeting of Korean Society of Mechanical Engineering.

Pham, T.-H., Nguyen, K., Park, H.C., 2023. A robotic fish capable of fast underwater swimming and water leaping with high Froude number. Ocean Engineering 268, 113512. https://doi.org/10.1016/j.oceaneng.2022.113512

Prempraneerach, P., F.S. Hover, Michael S. Triantafyllou., 2003. The effect of chordwise flexibility on the thrust and efficiency of a flapping foil, in: 13th Int. Symp. on Unmanned Untethered Submersible Technology: Special Session on Bioengineering Research Related to Autonomous Underwater Vehicles. New Hampshire, pp. 152–170.

Raj, A., Thakur, A., 2016. Fish-inspired robots: design, sensing, actuation, and autonomy—a review of research. Bioinspir Biomim 11, 031001. https://doi.org/10.1088/1748-3190/11/3/031001

Read, D.A., Hover, F.S., Triantafyllou, M.S., 2003. Forces on oscillating foils for propulsion and maneuvering. J Fluids Struct 17, 163–183. https://doi.org/10.1016/S0889-9746(02)00115-9

Ren, K., Yu, J., 2021. Research status of bionic amphibious robots: A review. Ocean Engineering 227, 108862. https://doi.org/10.1016/j.oceaneng.2021.108862

Rossi, C., Colorado, J., Coral, W., Barrientos, A., 2011. Bending continuous structures with SMAs: a novel robotic fish design. Bioinspir Biomim 6, 045005. https://doi.org/10.1088/1748-3182/6/4/045005

Salazar, R., Campos, A., Fuentes, V., Abdelkefi, A., 2019. A review on the modeling, materials, and actuators of aquatic unmanned vehicles. Ocean Engineering 172, 257–285. https://doi.org/10.1016/j.oceaneng.2018.11.047

Sfakiotakis, M., Lane, D.M., Davies, J.B.C., 1999. Review of fish swimming modes for aquatic locomotion. IEEE Journal of Oceanic Engineering 24, 237–252. https://doi.org/10.1109/48.757275

Shadwick, R.E., Syme, D.A., 2008. Thunniform swimming: muscle dynamics and mechanical power production of aerobic fibres in yellowfin tuna (*Thunnus albacares*). Journal of Experimental Biology 211, 1603–1611. https://doi.org/10.1242/jeb.013250

Tangorra, J., Phelan, C., Esposito, C., Lauder, G., 2011. Use of Biorobotic Models of Highly Deformable Fins for Studying the Mechanics and Control of Fin Forces in Fishes. Integr Comp Biol 51, 176–189. https://doi.org/10.1093/icb/icr036

Taylor, G.K., Nudds, R.L., Thomas, A.L.R., 2003. Flying and swimming animals cruise at a Strouhal number tuned for high power efficiency. Nature 425, 707–711. https://doi.org/10.1038/nature02000

Triantafyllou, M.S., Hover, F.S., Techet, A.H., Yue, D.K.P., 2005. Review of Hydrodynamic Scaling Laws in Aquatic Locomotion and Fishlike Swimming. Appl Mech Rev 58, 226–237. https://doi.org/10.1115/1.1943433

Triantafyllou, M.S., Triantafyllou, G.S., Gopalkrishnan, R., 1991. Wake mechanics for thrust generation in oscillating foils. Physics of Fluids A: Fluid Dynamics 3, 2835–2837. https://doi.org/10.1063/1.858173

Tsimbo Fokou, M.R., Xia, Q., Jin, H., Xu, M., Dong, E., 2023. A Soft Robotic Fish Actuated by Artificial Muscle Modules (SoRoFAAM-1). J Bionic Eng 20, 2030–2043. https://doi.org/10.1007/s42235-023-00390-6

Walters, V., Fierstine, H.L., 1964. Measurements of swimming speeds of yellowfin tuna and wahoo. Nature 202, 208.

Wang, T., Wen, L., Liang, J., Wu, G., 2010. Fuzzy vorticity control of a biomimetic robotic fish using a flapping lunate tail. J Bionic Eng 7, 56–65. https://doi.org/10.1016/S1672-6529(09)60183-9

Webb, P.W., 1988. Simple physical principles and vertebrate aquatic locomotion. Am Zool 28, 709–725. https://doi.org/10.1093/icb/28.2.709

Wen, L., Liang, J., Wu, G., Li, J., 2010. Hydrodynamic Experimental Investigation On Efficient Swimming Of Robotic Fish Using Self-propelled Method, in: In ISOPE International Ocean and Polar Engineering Conference (Pp. ISOPE-I). ISOPE. Beijing, China.

Wen, L., Wang, T., Wu, G., Liang, J., 2013. Quantitative thrust efficiency of a self-propulsive robotic fish: experimental method and hydrodynamic investigation. IEEE/ASME Transactions on Mechatronics 18, 1027–1038. https://doi.org/10.1109/TMECH.2012.2194719

White, C.H., Lauder, G. V, Bart-Smith, H., 2021. Tunabot Flex: a tuna-inspired robot with body flexibility improves high-performance swimming. Bioinspir Biomim 16, 026019. https://doi.org/10.1088/1748-3190/abb86d

Youssef, S.M., Soliman, M., Saleh, M.A., Elsayed, A.H., Radwan, A.G., 2022. Design and control of soft biomimetic pangasius fish robot using fin ray effect and reinforcement learning. Sci Rep 12, 21861. https://doi.org/10.1038/s41598-022-26179-x

Yu, C., Liu, Mengfei, Zhang, C., Yan, H., Zhang, M., Wu, Q., Liu, Mingjie, Jiang, L., 2020. Bio-inspired drag reduction: From nature organisms to artificial functional surfaces. Giant 2, 100017. https://doi.org/10.1016/j.giant.2020.100017

Yu, J., Zhang, C., Liu, L., 2016. Design and Control of a Single-Motor-Actuated Robotic Fish Capable of Fast Swimming and Maneuverability. IEEE/ASME Transactions on Mechatronics 21, 1711–1719. https://doi.org/10.1109/TMECH.2016.2517931

Yu, Y.-L., Huang, K.-J., 2021. Scaling law of fish undulatory propulsion. Physics of Fluids 33. https://doi.org/10.1063/5.0053721

Zhong, Q., Zhu, J., Fish, F.E., Kerr, S.J., Downs, A.M., Bart-Smith, H., Quinn, D.B., 2021. Tunable stiffness enables fast and efficient swimming in fish-like robots. Sci Robot 6, eabe4088. https://doi.org/10.1126/scirobotics.abe4088

Zhong, Y., Li, Z., Du, R., 2017. A novel robot fish with wire-driven active body and compliant tail. IEEE/ASME Transactions on Mechatronics 22, 1633–1643. https://doi.org/10.1109/TMECH.2017.2712820

Zhu, J., White, C., Wainwright, D.K., Di Santo, V., Lauder, G. V., Bart-Smith, H., 2019. Tuna robotics: A high-frequency experimental platform exploring the performance space of swimming fishes. Sci Robot 4, eaax4615. https://doi.org/10.1126/scirobotics.aax4615